

**Effect of Oxygen Storage Materials on the Performance of Pt-based Three-Way Catalysts**

Journal:	<i>Catalysis Science & Technology</i>
Manuscript ID	CY-ART-03-2022-000469.R1
Article Type:	Paper
Date Submitted by the Author:	13-Apr-2022
Complete List of Authors:	Wang, Gang; Hokkaido University Jing, Yuan; Hokkaido University Ting, Kah Wei; Hokkaido university, Catalysis Research Center Maeno, Zen; Hokkaido University, Institute for Catalysis Zhang, Xiaorui; Johnson Matthey Japan GK Sakura Nagaoka, Shuhej; Johnson Matthey Japan GK Shimizu, Ken-ichi; Hokkaido University, Catalysis Research Center Toyao, Takashi; Hokkaido university, Institute for Catalysis

Effect of Oxygen Storage Materials on the Performance of Pt-based Three-Way Catalysts

Gang Wang,[†] Yuan Jing,[†] Kah Wei Ting,[†] Zen Maeno,[†] Xiaorui Zhang,[§] Shuhei Nagaoka,^{*§}
Ken-ichi Shimizu^{†,‡}, and Takashi Toyao^{*†,‡}

[†] Institute for Catalysis, Hokkaido University, N-21, W-10, Sapporo 001-0021, Japan

[§] Johnson Matthey Japan G.K., 5123-3, Kitsuregawa, Sakura, Tochigi 329-1412, Japan

[‡] Elements Strategy Initiative for Catalysts and Batteries, Kyoto University, Katsura, Kyoto 615-8520, Japan

Corresponding authors: Takashi Toyao and Shuhei Nagaoka

E-mail: toyao@cat.hokudai.ac.jp; Shuhei.Nagaoka@mattheyasia.com

ABSTRACT The cost of Pt is currently lower than that of Pd and Rh, however, Pt-based three-way catalysts (TWCs) have attracted less attention than Pd- and Rh-based TWCs. Consequently, the fundamental understanding of the properties of Pt-based TWCs remains insufficient. Herein, we demonstrate the effect of oxygen storage materials (OSMs), including CeO₂ and CeO₂-ZrO₂ solid-solutions having different ceria contents (20%, 45%, and 66%), on the three-way catalysis performance of Pt/OSMs using various spectroscopic observations in combination with kinetic studies. In comparative assessments of powdered and monolithic (honeycomb) catalysts, fresh Pt/OSM(100%CeO₂) and aged Pt/OSM(66%CeO₂) exhibited the highest NO conversion among their corresponding series, showing that Pt/OSM(66%CeO₂) is the most promising and stable among the TWCs. *In situ* CO adsorption infrared (IR) spectroscopy and X-ray photoelectron spectroscopy (XPS) revealed that the Pt⁰ species loaded on OSMs having a higher ceria content were more electron-deficient. *Operando* IR and kinetic investigations suggested that increasing the ceria content in fresh Pt/OSMs enhanced not only the formation of nitrite species and their reactivity toward CO but also the resistance to CO poisoning during NO–CO reactions. *In situ* X-ray absorption spectroscopy (XAS) indicated that both Ce and Pt species in Pt/OSM catalysts are involved in NO–CO reactions through their redox cycles. *In situ* XAS in combination with X-ray diffraction (XRD) measurements revealed that the hydrothermal ageing treatment resulted in the aggregation of Pt particles and lattice contraction of CeO₂ in Pt/OSMs, causing severe degradation of the redox ability of Pt and Ce species and reducing the promoting effect of ceria on the formation of nitrites and their reactivity toward CO.

KEYWORDS: *three-way catalysis (TWC), oxygen storage materials (OSM), Platinum, in situ/operando spectroscopy*

1. Introduction

Regulations on vehicular emissions of hydrocarbons (HCs), carbon monoxide (CO), and nitrogen oxides (NO_x) are becoming increasingly stringent worldwide. Significant efforts have been devoted to the development of three-way catalysis (TWC), which is considered as one of the effective technologies for the abatement of exhaust gases^{1–7}. In the past few decades, a variety of metal-based catalytic materials have been designed and explored, including platinum group metals (PGMs) and non-noble metals (so-called base metal catalysts) such as Ni, Cu, and Fe. Base metal catalysts have largely been explored to evade the issues arising from the high cost and low availability of noble metals^{8–11}. Although base metals catalysts have excellent potential, they lack the intrinsic reactivity and durability required for automotive applications. Consequently, a practical system requires large amounts of PGMs to satisfy strict regulations^{12–21}.

Contemporary commercial TWCs are generally composed of Pd and a relatively small amount of Rh^{22–25}. Although Pd- and Rh-based TWCs deliver excellent catalytic performance, their application has been hindered in the recent years by the increasing price of Pd and Rh. Pt is currently less expensive than Pd and Rh, which incentivizes the use of Pt in place of Pd and Rh. However, Pt-based TWCs have attracted less attention than Pd- and Rh-based TWCs^{26–30}. Therefore, the design and development of effective catalytic supports is urgently required to improve the activity and stability of Pt-based TWCs to replace Pd- and Rh-based TWCs or reduce their use.

Compared to Al₂O₃-based commercial TWC supports^{31–35} and other promising metal oxide supports^{36,37}, oxygen storage materials (OSMs) such as CeO₂ and CeO₂-ZrO₂ solid-solutions are effective for control of air-fuel ratios (AFRs) that deviate from the stoichiometric conditions ($\lambda = 1$) in real-world applications; that is because OSMs possess excellent oxygen storage capacity (OSC) due to the rapid redox reaction of Ce, between its 4+ and 3+ oxidation states^{38–47}. Introducing the Zr⁴⁺ cation into the lattice of CeO₂ increases the concentration of structural defects, improves the oxygen mobility, and enhances the Ce³⁺/Ce ratio on the surface of PGM-based catalysts, producing more oxygen vacancies and Ce in the Ce³⁺ state^{48–51}. Note that such structural defects should only be local perturbation and the overall structure should be homogeneous on average as the dynamic oxygen

mobility in Pt/CeO₂-ZrO₂ catalysts was proportional to the structural homogeneity arising from the introduction of Zr into the CeO₂ framework⁵². Metal-support interactions (MSIs) and the adsorption and activation of TWC reactants occurring on OSM surfaces also influence the performance of OSMs^{53–57}. Wakita and co-workers concluded that the structural disorder in cubic Ce_{0.5}Zr_{0.5}O₂, which provides bulk diffusion paths for oxygen ions, was a possible factor contributing to its higher catalytic activity than that of CeO₂⁵⁸. Fan and co-workers discovered that the strong metal-support interaction (SMSI), which could be modulated under the oxidative/reductive atmosphere, influenced the structure and performance of Pt/Ce_{0.67}Zr_{0.33}O₂, and samples with a weaker SMSI exhibited higher conversion of NO and CO⁵⁹. Nagai and co-workers reported that the Pt–O–Ce bond formed by the Pt–oxide–support interaction acted as an anchor and inhibited the agglomeration of Pt particles under oxidizing conditions at high temperatures⁶⁰. Nunan and co-workers discovered that the degree of Pt/Ce interaction and the resulting activity could be controlled by varying the CeO₂ crystallite size. Reducing the CeO₂ crystallite size increased the Pt/Ce interaction, thereby increasing the activity of fresh and aged catalysts⁶¹. These are seminal findings in this area of research. However, the fundamental understanding of the properties of OSMs and their effects on the performance of Pt-based TWCs remains insufficient, particularly under conditions relevant to modern three-way catalysis operations, where deviations from stoichiometric conditions (i.e., fuel cut and acceleration) are often encountered. Comprehensive studies are required to further understand the behavior of Pt catalysts loaded on OSM supports during three-way catalysis.

In this study, we further investigated the effect of OSMs on the catalytic performance of Pt-based TWCs. In catalytic evaluations of powdered and monolithic honeycomb catalysts, fresh Pt/OSM(100%CeO₂) and aged Pt/OSM(66%CeO₂) delivered the highest performance among the corresponding sample series. The results of various kinetic and spectroscopic studies, including *in situ (operando)* Fourier transform infrared (FT-IR) spectroscopy, X-ray absorption spectroscopy (XAS), and X-ray photoelectron spectroscopy (XPS), proved that the presence of electron-deficient Pt⁰ in combination with the excellent redox properties of the Pt and Ce species present in the Pt/OSM catalyst increased the conversion of NO and effectively inhibited poisoning by CO.

2. Experimental Section

2.1 Preparation of Catalysts

He (purity >99.995%), H₂ (purity >99.99%), O₂ (purity >99.5%), N₂ (purity >99.99%), Ar (purity >99.99%), NO (purity >99.5%), CO (purity >99.95%), CO₂ (purity >99.99%), C₃H₆ (purity >99.95%) gases were obtained from Air Water Inc. and were used for catalyst preparations, catalytic reactions using powdered catalysts, and *in situ/operando* experiments. For catalysts ageing under hydrothermal redox conditions and catalytic reactions using honeycomb catalysts, purities of gases used were as follows; >99.9999% for H₂, >99.5% for O₂, >99.0% for NO, >99.9% for CO, >99.5% for CO₂, and 99.9999% for C₃H₆. Pt-based TWCs (Pt/OSMs; 3 wt% Pt) were prepared using commercially available CeO₂ or CeO₂-ZrO₂ mixed oxide powders according to the following impregnation procedure. An OSM powder (5 g) and an aqueous solution (100 mL) containing 0.247 g (0.769 mmol) of Pt(NH₃)₂(NO₂)₂ which dissolved in HNO₃ (Pt content = 4.6 wt.%; Furuya Metal Co., Ltd.) were charged in a 500 mL glass vessel. The mixed solution was stirred for 15 min at room temperature prior to rotary evaporation at 50 °C and drying at 90 °C in an oven for 12 h. Subsequently, the as-obtained solids were calcined in a furnace at 500 °C in a static air atmosphere for 3 h. Prior to catalytic evaluation and *operando/in situ* spectroscopic experiments, the catalyst samples were reduced in a flow of 10% H₂/He (100 mL/min) at 400 °C for 30 min.

Monolithic honeycomb catalysts were fabricated by coating a slurry, prepared from calcined catalyst powders, an inactive alumina-based inorganic binder, and water, onto a cordierite honeycomb (25.4 mm × 50 mm, 400 cells/in²; NGK Insulators, Ltd.), followed by drying at 120 °C in air for 1 h and calcination at 600 °C for 2 h. The as-obtained honeycomb catalysts contained approximately 60 g/L Pt/OSM solids, amounting to a total Pt loading of 0.18 g/L.

The ageing of monolithic honeycomb catalysts was conducted at 1000 °C for 4 h under hydrothermal redox conditions under a perturbation cycle of 180 s (3% CO, 3% H₂, 10% H₂O, and 84% N₂), 10 s (10% H₂O and 90% N₂), 180 s (3% O₂, 10% H₂O, and 87% N₂), and 10 s (10% H₂O and 90% N₂), simulating rich, stoichiometric, lean, and stoichiometric atmospheres, respectively. The total flow rate of the feed gas was 3 L/min, which corresponds to a space velocity of 7200 h⁻¹. The

aged powder catalysts used for characterization were obtained through exposing the powder catalysts to the hydrothermal redox conditions. Equivalency of the thermal stress toward the catalysts between the lab-redox and engine ageing was confirmed by similarity of the specific surface areas for the two aged catalysts.

2.2 Catalyst Characterization

Physical N₂ adsorption measurements were conducted using AUTOSORB 6AG (Yuasa Ionics Co., Ltd., Japan). X-ray diffraction (XRD) patterns were recorded using Cu-K α radiation on a Miniflex benchtop X-ray diffractometer (Rigaku Corp., Japan) under ambient conditions. High-angle annular dark-field scanning transmission electron microscopy (HAADF-STEM) and energy dispersive X-ray spectroscopy (EDX) were performed using an FEI Titan G2 80-300 electron microscope. CO adsorption experiments were performed at -70 °C and -185 °C using a BELCAT II apparatus (MicrotracBEL Corp., Japan). Temperature-programmed reduction by H₂ (H₂-TPR) was also performed using the BELCAT I equipment (MicrotracBEL Corp., Japan). Samples (20 mg) were placed in a U-type quartz cell and heated to 850 °C at a rate of 15 °C/min in a flow of 5% H₂/Ar (100 mL/min). The residual H₂ in the outlet gas was quantified using a thermal conductivity detector (TCD) following the removal of water by passing the outlet gas through a 4 Å molecular sieve. XPS characterization of the reduced catalyst specimens was performed on a ESCA-3400HSE spectrometer (Shimadzu, Japan) using Mg-K α (1253.6 eV) radiation. The samples were prepared in a glove box prior to being connected to the XPS chamber to avoid exposure to air. The binding energies were calibrated with respect to C_{1s} at 285.0 eV. CO adsorption IR experiments for fresh catalysts were conducted at -185 °C after reduction in a flow of 10% H₂/He (20 mL/min) at 400 °C for 30 min. The stream of 1% CO/He (10 mL) was introduced to the catalyst pellet (ϕ = 13 mm) until the intensity of CO adsorption peak was unchanged, followed by evacuation to remove the physically adsorbed CO on the catalyst. The IR spectra were then recorded.

2.3 Operando IR

Operando IR spectroscopic measurements during NO–CO reactions on fresh and aged Pt/OSMs having varying ceria contents were conducted at 200 °C on an FT/IR-4200 spectrometer (JASCO,

Japan) equipped with a mercury-cadmium-telluride (MCT) detector. Typically, catalyst pellets ($\phi = 13$ mm) pressed using 40 mg samples were charged in a quartz IR cell equipped with CaF_2 windows and a gas line system, and thereafter reduced in a flow of 10% H_2/He (100 mL/min) at 400 °C for 30 min prior to testing. Following the cooling of each pellet to 200 °C in a flow of He, 0.5% NO/He (80 mL/min) was introduced into the cell for 10 min prior to reverting to He flow to purge the residual NO inside the cell. Thereafter, 0.5% CO/He (80 mL/min) was flown into the cell for 10 min. The gas composition at the outlet was identified and quantitatively analyzed using an FT-IR gas cell (JASCO FT/IR-4100) and a 490 Micro gas chromatograph (GC, Agilent Technologies Inc., USA) equipped with MS5A (10 m) and PoraPLOT Q (10 m) columns and a high-sampling-rate TCD. The background of the IR spectrum was subtracted from the reference recorded at 200 °C in a flow of He.

2.4 (*In situ*) XAS

All the XAS spectra were recorded in the transmittance mode at the BL14B2 beamline of SPring-8 (proposals 2020A1695 and 2021A1615). A Si (311) double crystal monochromator was used for the Pt L_3 -edge, Zr K-edge, and Ce K-edge measurements, whereas a Si (111) double crystal monochromator was used for the Ce L_3 -edge measurements. Data analysis was conducted using Athena software ver. 0.9.25, which was included in the Demeter package.

For *ex situ* studies, including measurements of reference compounds, samples in pellet form ($\phi = 10$ mm) were sealed in a polyethylene cell in air, and their spectra were recorded at ambient temperature. For *in situ* studies, samples in pellet form ($\phi = 7$ mm; mixed with boron nitride (BN) if necessary) were placed in a quartz cell equipped with Kapton film windows and gas lines. For H_2 -TPR, upon the introduction of 10% H_2/He (1000 mL/min), the cell was heated to 850 °C at a ramp rate of 15 °C/min. For the NO–CO reactions, the catalyst was reduced in a 10% H_2/He (100 mL/min) flow at 400 °C for 30 min and thereafter cooled to 200 °C. Subsequently, 0.5% NO/He , 0.5% CO/He , or 0.5% $\text{NO} + 0.5\%\text{CO}/\text{He}$ were introduced into the cell. The spectra of standard CeO_2 and $\text{Ce}(\text{NO}_3)_3$, and PtO_2 and Pt foil were used as references for the quantification of the corresponding species (Ce^{4+} and Ce^{3+} , Pt^{4+} and Pt^0) using the linear combination fitting (LCF) method. Note that the LCF analysis provides information about only relative changes because the reference spectra do not exactly match

spectra of the main samples even if the formal oxidation states are the same.

2.5 Catalytic Reactions

Catalytic NO–CO reactions on fresh and aged Pt/OSMs having different ceria contents were performed in a fixed-bed flow reactor. Briefly, 20 mg of catalyst powder was charged in a tubular reactor using quartz wool to fix the layer, followed by reduction in a flow of 10% H₂/He (100 mL/min) at 400 °C for 30 min prior to commencing the reaction. Upon reaching the required temperature, a flowing gas mixture containing 0.5% NO and 0.5% CO in He was supplied at 80 mL/min (*F/W* corresponds to 4000 mL/g_{Cat}/min). The gas composition in the outlet was quantitatively analyzed by a GC equipped with a SHINCARBON ST column (Shimadzu GC-8A) to determine the conversions and yields according to the following chemical equations:



Kinetic studies of fresh and aged Pt/OSMs having different ceria contents were carried out under controlled conditions when the conversion was below 10%. The apparent reaction order with respect to NO (CO) was determined from the steady-state reaction rates measured in a stream having different partial pressures of NO (CO) while maintaining a constant CO (NO) content. The activation barrier was determined from the steady-state reaction rates measured at different temperatures. The elimination of mass transfer limitation was confirmed using the Mears criterion for external diffusion and the Weisz-Prater criterion for internal diffusion, which are expressed in equations (3) and (4) ⁶².

$$\frac{-r'_A \rho_b R n}{k_c C_A} < 0.15 \quad (3)$$

where $-r'_A$, ρ_b , R , n , k_c , and C_A are the reaction rate, bulk density of the catalyst bed, catalyst particle radius, reaction order, mass transfer coefficient, and reactant concentration, respectively. If the value of the term on the left-hand side is lower than 0.15, the external mass transfer effects can be neglected.

$$C_{WP} = \frac{-r'_A \rho_c R^2}{D_e C_A} < 1 \quad (4)$$

where $-r'_A$, ρ_c , R , D_e , and C_A are the reaction rate, catalyst density, catalyst particle radius, effective gas-phase diffusivity, and concentration of reactant A at the catalyst surface, respectively. If the value

of C_{WP} is lower than 1, the internal mass transfer effects can be ignored.

Catalytic reactions on the honeycomb catalysts were conducted using a MEXA-series emission measurement system (Horiba Ltd., Japan). The catalysts were charged in a tubular reactor, and their catalytic performance was evaluated by feeding a gas mixture consisting of CO, C₃H₆, H₂, NO, O₂, CO₂, and H₂O (with the remainder being N₂) at different values of lambda at a space velocity (SV) of 100,000 h⁻¹. The value of lambda was calculated according to equation (5) (see **Tables S1-S3** for further details on the gas compositions for the corresponding experiments). Prior to each catalytic activity test, the honeycomb catalyst was pre-treated in a flow of the reaction gas (1 Hz perturbation between $\lambda = 0.95$ and $\lambda = 1.05$) at 400 °C for 30 min, followed by cooling to 100 °C in a flow of N₂. Conversions of NO, CO, and C₃H₆ were monitored using an exhaust gas analyzer (ABB, AO-2020).

$$\lambda = \frac{O_2 + 0.5CO + 0.5H_2O + CO_2 + 0.5NO}{0.5H_2 + CO + 1.5C_3H_6 + 0.5H_2O + CO_2} \quad (5)$$

3. Results and Discussion

3.1 Catalyst Characterization

BET surface areas (S_{BET}) were determined for fresh and aged Pt/OSMs having different ceria contents based on the results of N_2 adsorption experiments (**Figure S1**). **Figure 1** shows that the S_{BET} of the fresh catalyst increased as the ceria content increased; however, the S_{BET} of the corresponding samples following ageing exhibited an inverse trend. In addition, the ratio between the S_{BET} of the aged specimen and that of the fresh specimen decreased significantly with an increase in the ceria content, particularly for Pt/OSM(100%CeO₂), indicating the sintering of the support during hydrothermal ageing and the low thermal stability of CeO₂. **Figures 2** and **S2** depict the morphology and elemental distribution obtained from the EDS mapping of fresh and aged Pt/OSMs having different ceria contents. The zirconium introduced was dispersed uniformly with Ce in the fresh and aged catalysts having 20%, 45%, and 66% ceria. These results indicated the structure of ZrO₂-CeO₂ solid-solution is not destroyed, because no segregation of ZrO₂ from CeO₂ was observed after ageing, which was also confirmed by the XRD characterization. Furthermore, the support did not appear to be compacted, and the Pt particles were uniformly dispersed throughout the fresh catalyst samples. The textual properties calculated from CO-adsorption and STEM measurements, including S_{BET} and the average Pt particle size of fresh and aged Pt/OSMs having different ceria contents are summarized in **Table S4**. Please note that negligible amounts of CO were adsorbed on the aged samples. The aggregation of Pt particles (~9.0 nm) accompanied by the sintering of support was reflected by the change in the average Pt particle size and S_{BET} following hydrothermal ageing, compared with the fresh samples. Therefore, it can be obtained that the hydrothermal aging treatment will lead to the sintering of CeO₂, which can be alleviated by the introduction of ZrO₂, and aggregation of Pt particles.

Figures 3A and **3B** show the XRD patterns of fresh and aged Pt/OSMs having different ceria contents, respectively. The patterns exhibited by the fresh and aged samples correspond to cubic fluorite-type CeO₂ and CeO₂-ZrO₂ solid-solutions having different Ce/Zr ratios. The XRD peaks shifted to higher 2θ values with increasing zirconia content, revealing the contraction of the CeO₂ crystal

lattice⁶³. The absence of peaks attributed to the ZrO_2 and CeO_2 phases and of asymmetric reflections appearing in the fresh and aged samples with increasing zirconia content indicates a homogeneous solid-solution. No peaks attributable to Pt species were observed in the fresh specimens, owing to the small crystallite size and uniform dispersion of Pt on the support. Following hydrothermal ageing, peaks attributable to Pt species were observed in the XRD patterns of all samples, indicating the agglomeration of Pt crystallites at high temperatures. In addition, all reflections from the aged samples became sharper and narrower with increasing ceria content, indicating enhanced lattice contraction and powder sintering, which is consistent with the changes in the S_{BET} and the HAADF-STEM characterization results. In particular, the peak splitting appearing at $2\theta = 69.6^\circ$, 76.9° and 79.3° in the diffraction pattern of aged Pt/OSM(100%CeO₂) (**Figure S3**) revealed the ceria has grown in size leading to very narrow line widths^{64,65}. However, this phenomenon was not observed in the other aged samples, indicating that the introduced zirconia suppresses the sintering of ceria, which has been extensively investigated previously⁶⁶. In addition, the solid-solution structure of ZrO_2 - CeO_2 in aged samples can be still maintained even after hydrothermal treatment at 1000 °C.

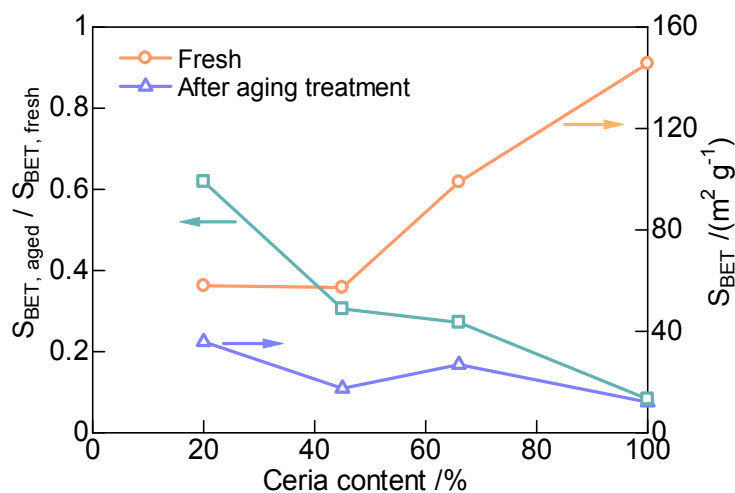


Figure 1. S_{BET} of fresh ($S_{\text{BET, fresh}}$) and aged ($S_{\text{BET, aged}}$) Pt/OSMs having different ceria content and the ratios of $S_{\text{BET, aged}}$ to $S_{\text{BET, fresh}}$.

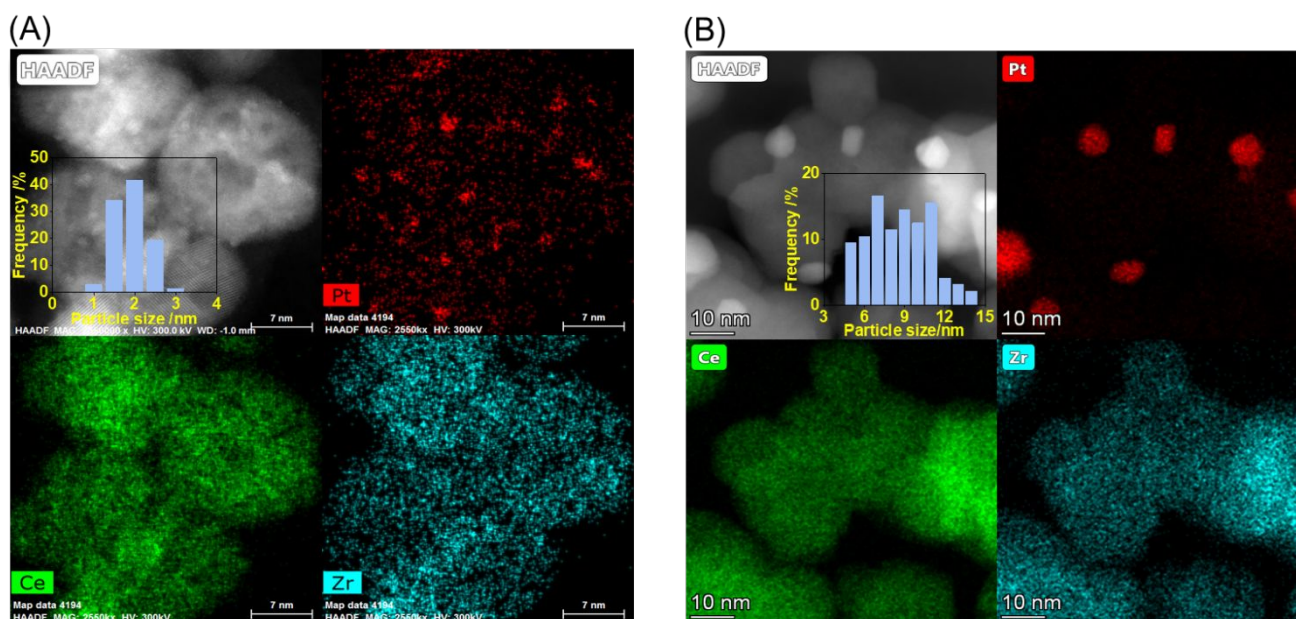


Figure 2. HAADF-STEM images and EDS elemental maps of (A) fresh and (B) aged Pt/OSMs(66%CeO₂).

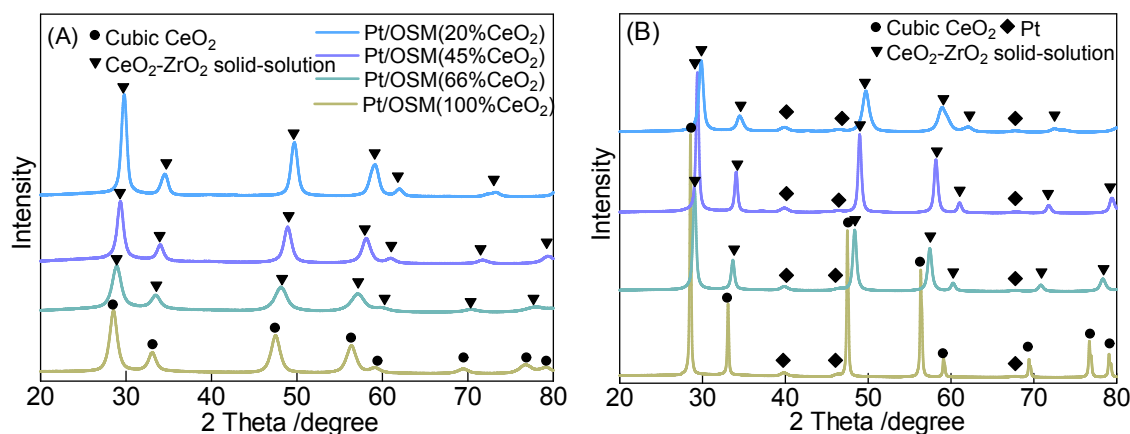


Figure 3. XRD patterns of (A) fresh and (B) aged Pt/OSMs having different ceria content.

The Zr K-edge X-ray absorption near-edge structure (XANES) spectra of the fresh and aged Pt/OSMs and their reference compounds, including ZrO₂ and Zr foil, are shown in **Figure S4**. The edge position of the XANES of the Pt/OSM samples corresponds closely to that of ZrO₂ used as a reference, indicating that zirconium species in Pt/OSMs exist as Zr⁴⁺. **Figure S5** depicts the Ce K-edge XANES spectra of the fresh and aged Pt/OSMs as well as their reference materials, CeO₂ and Ce(NO₃)₃. No difference was evident between the fresh and aged samples and the edge position corresponds well to that of a reference CeO₂ sample, suggesting the local structure of Ce in these specimens was similar to that in CeO₂. **Figures 4A and S6A** show the Ce L₃-edge XANES spectra and the evolution of Ce species during the H₂-TPR of OSM(66%CeO₂) and OSM(100%CeO₂) supports. The reduction of Ce⁴⁺ to Ce³⁺, indicated by the gradual disappearance of the characteristic

double-peak feature at ~5730 and ~5737 eV and the appearance of a sharp peak at ~5725 eV, can be identified from the XANES spectra^{67–69}. The well-known two-step reduction profile can be observed in these two samples, which assists in distinguishing between surface and bulk reduction^{70,71}, and the Ce⁴⁺ was completely reduced to Ce³⁺ at 800 °C. With the introduction of zirconia into the OSMs (**Figure S7A**), the bulk reduction peak shifted to a lower temperature (~560 °C) compared to that of CeO₂ (~710 °C). This is attributed to the ability of zirconia to introduce sublattice oxygen into the CeO₂-ZrO₂ solid-solution, generating defective structures and highly mobile oxygen atoms in the lattice that could be released at moderate temperatures^{72,73}. In particular, a single reduction peak can be noticed in the samples having lower ceria contents, OSM(25%CeO₂), and OSM(45%CeO₂), similar experimental phenomenon was also observed by Kašpar on the Ce_{0.5}Zr_{0.5}O₂ and Ce_{0.4}Zr_{0.6}O₂ samples during H₂-TPR⁷⁴. Following the loading of Pt species, an intense peak appeared at ~95 °C, which is attributed to the reduction of Pt oxide species, as shown in **Figures 4B** and **S6B**. The peak at ~337 °C would be with respect to the concomitant reduction of PtO_x and Ce⁴⁺, with the main contribution coming from the Ce component. A broad peak appearing in the vicinity of 700 °C was attributed to the reduction of bulk ceria in PtO₂/OSM(66%CeO₂) and PtO₂/OSM(100%CeO₂). Compared to the pristine support, the reduction of surface Ce⁴⁺ commences at a lower temperature and a higher rate following the loading of Pt oxide species, resulting from the Pt⁰-induced hydrogen spillover effect^{75,76}. In the spectra of the PtO₂/OSM(20%CeO₂) and PtO₂/OSM(45%CeO₂) samples (**Figure S7B**), a single peak linked to the reduction of Ce⁴⁺ was observed, which corresponds to the reduction of their OSM supports. A similar reduction phenomenon was also observed for Rh₂O₃/OSMs and PdO/OSMs having different ceria contents^{77,78}. However, no significant gradual changes were observed in the Zr K-edge XANES spectra except for slight fluctuations caused by the reduction of ceria (**Figure S8**), suggesting that the oxidation state of all Zr species in the OSM supports and the PtO₂/OSM samples during H₂ reduction remains constant at a formal valency of 4+. Thus, it can be concluded that the Ce⁴⁺ in ZrO₂-CeO₂ solid-solution can be reduced to Ce³⁺ accompanied with the reduction of Pt⁴⁺ to Pt⁰, however, the Zr⁴⁺ keeps unchanged.

XPS characterization and IR spectroscopy in conjunction with CO-adsorption experiments were carried out to assess the electronic properties of Pt particles in fresh and aged Pt/OSMs with different

ceria contents. **Figures 5A and 5B** show the Pt 4f XPS spectra of fresh and aged Pt/OSM specimens, respectively, following reduction using H₂ without exposure to air. Two signals at binding energies of ca. 71 and 74 eV attributed to metallic Pt were observed in these spectra⁷⁵. For the fresh samples, the signals shifted to lower binding energies as the ceria content decreased, suggesting that the Pt⁰ species were more electron-rich in Pt/OSMs having a lower ceria content. Following the ageing treatment, the Pt⁰ species in Pt/OSM(66%CeO₂) became the most electron-deficient, followed by those in Pt/OSM(45%CeO₂), Pt/OSM(20%CeO₂), and Pt/OSM(100%CeO₂). **Figure 5C** presents the *in situ* IR spectra recorded during the adsorption of CO onto fresh Pt/OSMs. The peak appearing at approximately 2070 cm⁻¹ in all these spectra was assigned to CO bound to the on-top sites of the metallic surfaces⁷⁹. The center of the peak gradually shifted to a higher wavenumber as the ceria content increased. And no peaks related to the CO adsorption on Zr⁴⁺/Ce⁴⁺ (~2150 cm⁻¹) and Ce³⁺ (2130-2120 cm⁻¹) sites were observed. The π back-donation from the transition metal surface to the 2 π^* antibonding orbital of the adsorbate (CO) is the principal contributor to the strength of adsorption^{80,81}. This contribution is weakened when Pt is positively charged, leading to a weaker adsorption of CO on the surface and less activation of adsorbed CO, resulting in a blue-shift of the peak center⁸². Therefore, it can be believed that the increasing ceria content in support favors the formation of more electron-deficient metallic Pt⁰ species in fresh Pt/OSM samples. This effect of the support on the electron structure of the loaded metal was also observed in Pd/M/Al₂O₃ (M = La, Ba, or Sr) TWCs in our previous studies^{83,84}.

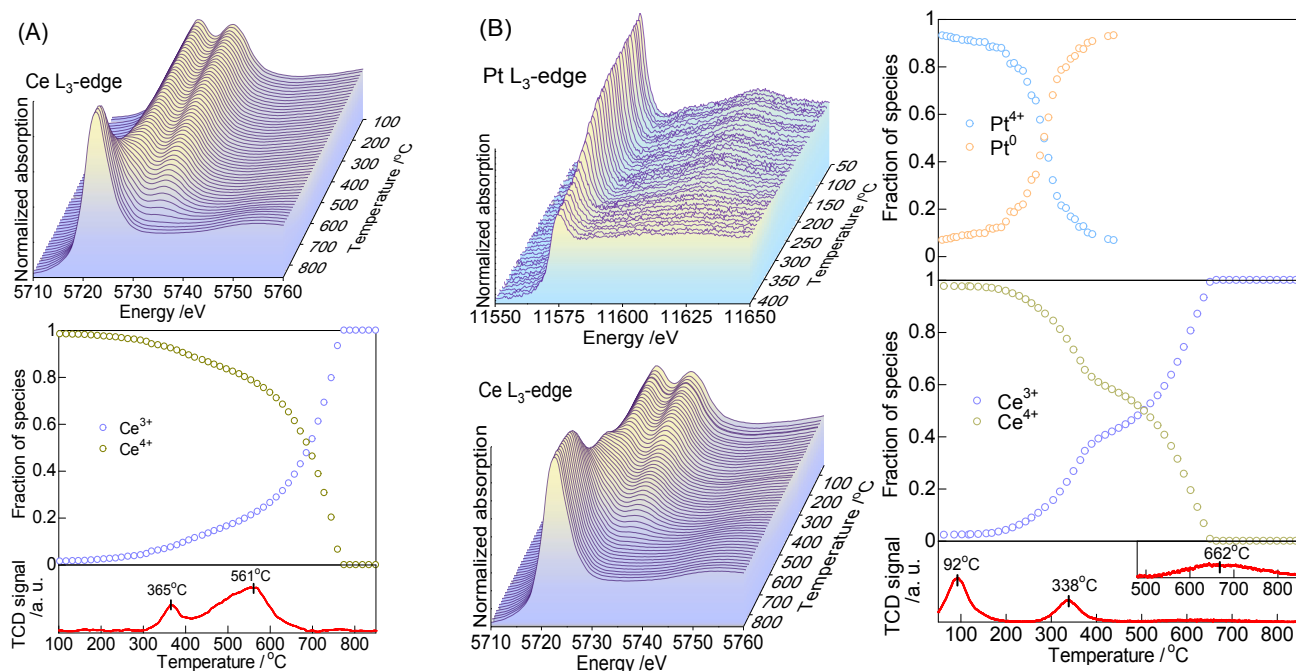


Figure 4. *In situ* Ce and Pt L₃-edge XAS during H₂-TPR of (A) OSM(66%CeO₂) (Sample amount = 1.9 mg with 20.4 mg of BN) and (B) PtO₂/OSM(66%CeO₂) (Sample amount = 2.0 mg with 20.4 mg of BN for Ce L₃-edge, and 21.8 mg with 12.8 mg BN for Pt L₃-edge measurements) conducted in H₂ flow (1000 mL/min) at the heating rate of 15 °C/min using CeO₂ and Ce(NO₃)₃, and Pt foil and PtO₂ as references for linear combination fitting analysis.

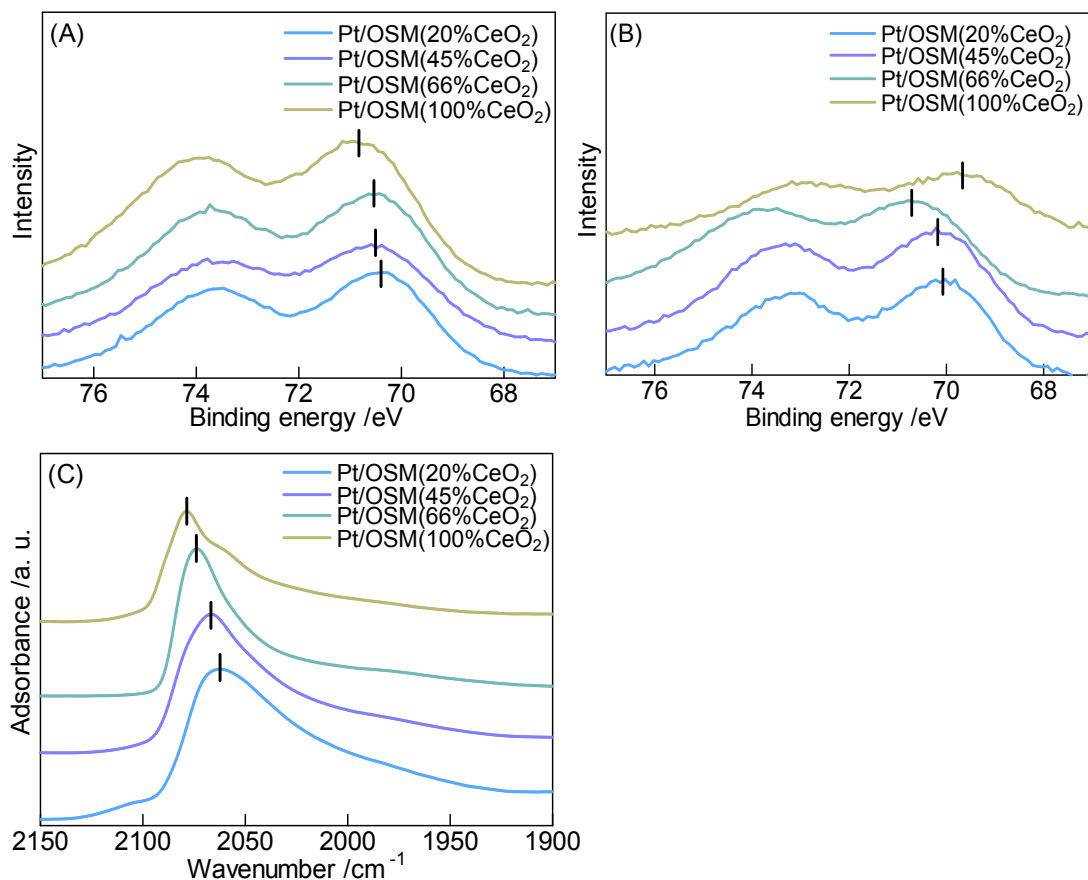


Figure 5. Pt 4f XPS spectra of (A) fresh and (B) aged Pt/OSMs. (C) *In situ* CO adsorption IR spectra of fresh Pt/OSMs following the reduction using H₂ without exposure to air.

3.2 Effect of OSMs on catalytic NO–CO reactions

NO–CO reactions were performed on fresh and aged powdered Pt/OSMs having different ceria contents, as shown in **Figure 6**. The catalytic activity was enhanced with the increase in the ceria content among the freshly tested catalysts, and Pt/OSM(100%CeO₂) delivered the highest performance. However, the catalytic performance followed the order Pt/OSM(66%CeO₂) > Pt/OSM(45%CeO₂) > Pt/OSM(20%CeO₂) > Pt/OSM(100%CeO₂) after ageing treatment, due to the thermal stability enhanced by the introduction of zirconia and the promotional effect of ceria in catalytic activity. These results verify that the ceria content of the OSM support significantly influences the catalytic performance of the as-prepared Pt/OSM in NO–CO reactions. In addition, the catalytic activity of Pt/OSMs decreased dramatically following the ageing treatment due to the aggregation of Pt particles and structural changes in the support. It should be noted that the main products are N₂O and CO₂ with mass balance of 100% in the relatively low temperature region (below 450 °C). Further, to investigate the effect of OSM support on the catalytic properties of Pt/OSM, the apparent reaction orders with respect to NO and CO, as well as the activation barrier, were determined for fresh and aged catalysts from the turnover frequencies (TOFs) in streams having different partial pressures of NO and CO (**Figure S9** and **Table S5**). The TOFs were determined using the steady-state reaction rates measured at NO conversions lower than 10% and CO adsorption amounts at -20 °C. Reactions involving CO are usually of a negative order with respect to the CO concentration on Pt-based catalysts^{85,86}; that is because the strong binding of CO to the surface of PGMs inhibits the catalyst, that is, CO serves as a catalyst poison. This phenomenon was also observed for both fresh and aged Pt/OSMs, for which the reaction order with respect to CO was negative, revealing that the strong adsorption of CO onto Pt particles suppressed the NO–CO reactions. By combining the calculated reaction order of CO and the IR and XPS characterization results recorded during the adsorption of CO, the extent to which CO inhibits the reaction can be attributed to the electronic properties of the supported Pt⁰ species; increased electron-deficiency reduces the inhibition caused by CO. Therefore, increasing the ceria content of the catalyst reduces poisoning by CO; however, this promoting effect is decreased by the sintering of ceria, as indicated by the fact that Pt/OSM(66%CeO₂) exhibits the strongest poisoning-resistance among all the aged catalysts. The Arrhenius plots indicate that the NO–CO reactions on fresh catalysts having higher ceria contents exhibit lower activation energies,

and the corresponding samples exhibit higher activation energies following the ageing treatment, which supports the catalytic evaluation results.

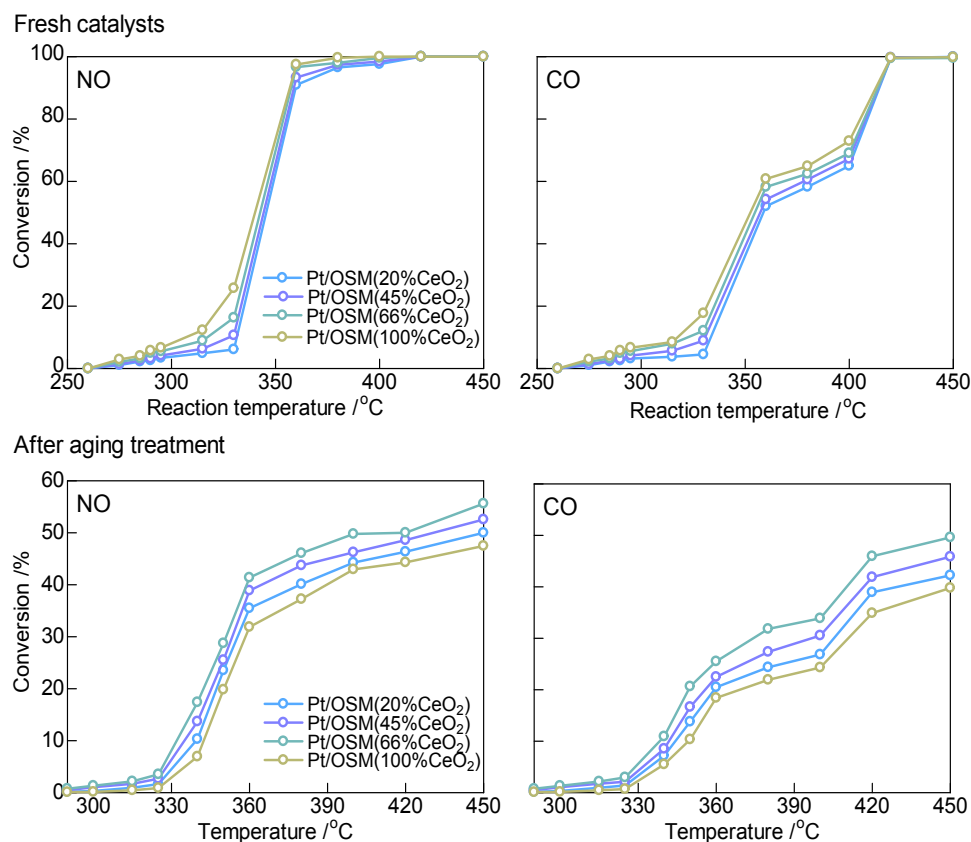


Figure 6. Effect of OSMs having different ceria contents on catalytic NO–CO reactions over powdered fresh and aged Pt/OSMs (20 mg) in a flow of 0.5% NO, 0.5% CO, and 99% He (80 mL/min).

To gain clearer insights into the effect of OSMs on the formation and evolution of surface species and their reactivity during NO–CO reactions on fresh and aged Pt/OSMs having different ceria contents, *operando* IR spectroscopic experiments were performed and the results are presented in **Figure 7**. Following exposure to NO, various NO_x species were formed on the catalyst surface as evidenced by the peaks appearing in the 1100–1700 cm⁻¹ region^{87,88}. Specifically, the peak at approximately 1170 cm⁻¹ was ascribed to the surface nitrite species^{89,90}. The intensity of this peak is higher in the fresh Pt/OSMs having a higher ceria content, indicating that ceria can efficiently promote the production of surface nitrite species. However, nearly no nitrite formation was observed on aged Pt/OSM(100%CeO₂), largely due to the heavy agglomeration of CeO₂ and sintering of Pt particles, as confirmed by N₂ adsorption, HAADF-STEM, and XRD characterizations. Besides, the hydrothermal aging treatment at 1000 °C can cause the strong metal-support interaction (SMSI) in aged catalysts and therefore the Pt particles can be wrapped or covered by Ce species^{56,91}, leading to the difficult

contact between Pt sites and reactant molecules and the consequential decrease in the intensity of IR absorption peaks of the aged samples. The broad bands in the region of 1250-1650 cm^{-1} were attributed to the characteristic absorption of nitrate species in different modes⁹². The peak at approximately 1781 cm^{-1} is ascribed to the NO species adsorbed on Pt particles, which can transform into N_2O and nitrite species through a disproportionation reaction⁹³. The bands emerging in the region of 1293-1606 cm^{-1} were assigned to carbonate species adsorbed on the catalyst surface, and, upon exposure to CO in a flow of 0.5% CO/He, gradually increased in intensity⁹⁴. However, the intensity of the peak attributed to nitrite species declined during the introduction of CO. As shown in the plots on the right-hand side of **Figure 7**, the rate of consumption of nitrite species, which reflects their reactivity, is enhanced by increases in the ceria content of fresh Pt/OSMs. However, the aged catalysts follow the order Pt/OSM(66%CeO₂) > Pt/OSM(45%CeO₂) > Pt/OSM(20%CeO₂) > Pt/OSM(100%CeO₂) with respect to the reactivity of nitrite species. Furthermore, the as-detected concentrations of N_2O and CO₂ changed in agreement with the reactivity trend. These results reveal that the efficient formation of nitrite species and their reactivity toward CO are crucial to NO–CO reactions on fresh and aged Pt/OSMs, and the increased ceria content in fresh samples can promote this process.

To understand the redox behaviors of Ce, Pt, and Zr species in fresh and aged catalysts during NO–CO reactions and their effects on catalytic performance, *in situ* Ce and Pt L₃-edge and Zr K-edge XAS measurements were conducted under consecutive flows of 0.5% NO/He and 0.5% CO/He, or a combined flow of 0.5%NO + 0.5%CO/He for the fresh and aged Pt/OSM(66%CeO₂) samples. The corresponding *in situ* Ce and Pt L₃-edge XANES spectra and the LCF analysis results are shown in **Figure 8**. The Ce³⁺ and Pt⁰ species in the fresh Pt/OSM(66%CeO₂) sample were oxidized upon the introduction of NO, as evidenced by the change in the intensity of the corresponding peak in the XANES spectra. The Pt species oxidized by NO could be completely reduced by exposure to CO flow; however, the Ce⁴⁺ species was only partially reduced to Ce³⁺, which could be re-oxidized by the subsequent NO flow. When the composition of the flowing gas was altered to 0.5%NO + 0.5%CO/He, the fractions of the Ce³⁺, Ce⁴⁺, and Pt⁰ species remained nearly unchanged. In contrast, the redox abilities of Ce and Pt species in the aged Pt/OSM(66%CeO₂) specimen were much lower than those in the fresh sample under identical conditions, and the oxidation of Ce³⁺ was easier than the reduction

of Ce^{4+} . This is because the hydrothermal ageing treatment causes the aggregation of Pt particles, lattice contraction of CeO_2 and progressive cubic crystallization of ZrO_2 , as confirmed by the HAADF-STEM, XRD, and XAS characterizations. The redox behavior of Pt can be correlated to the particle size; the larger particles are more difficult to oxidize^{95,96}. The lattice contraction of CeO_2 and the gradual cubic crystallization of ZrO_2 restrict the mobility of oxygen in the CeO_2 - ZrO_2 solid-solution, thereby suppressing the redox transition of Ce^{74,78}. Unlike Pt and Ce, no prominent redox transition was exhibited by zirconium in the fresh and aged samples, in which it remained in the formal oxidation state of Zr^{4+} (**Figure S10**). These results demonstrate that the Ce and Pt are both involved in NO-CO reactions through their redox cycles and abilities, which are affected by the structural properties and particle size changed by hydrothermal aging treatment, and are crucial to the catalytic activity in NO-CO reactions.

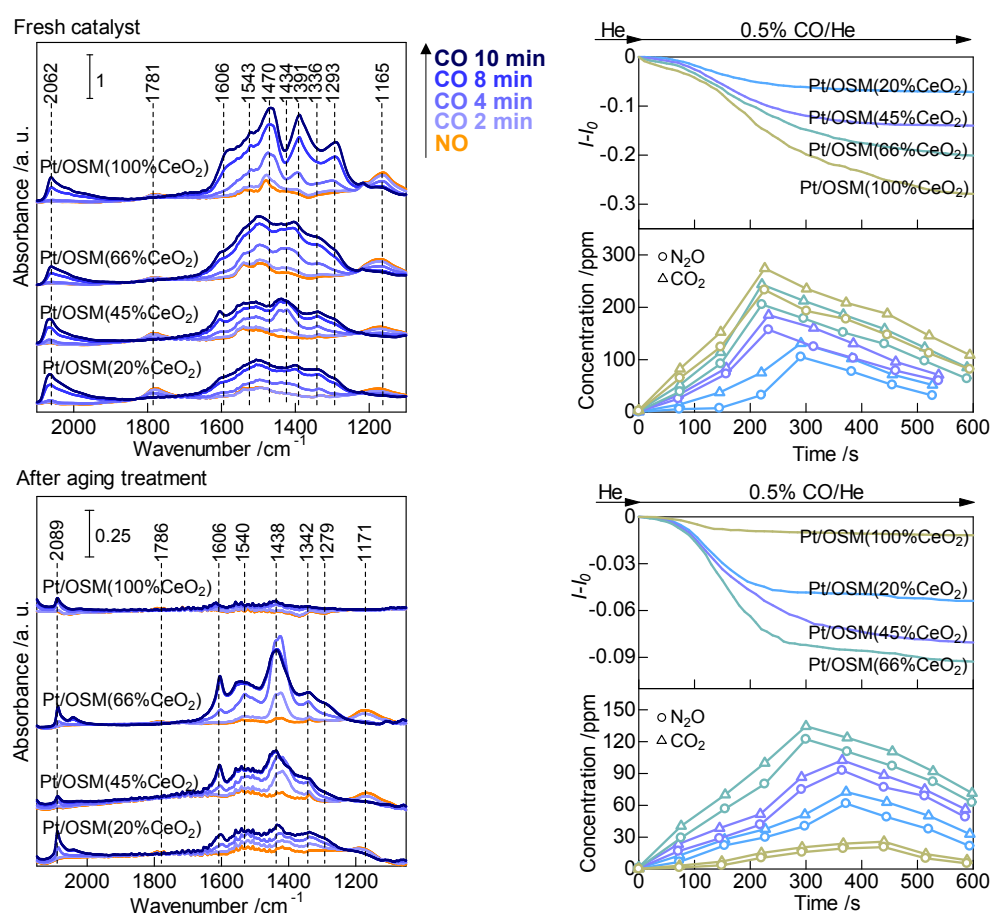


Figure 7. Results of *Operando* IR spectroscopic experiments performed to identify the formation of surface species and their reactivity toward CO on reduced fresh and aged Pt/OSMs recorded continuously following the introduction of 0.5% CO/He (seablue) after exposure to 0.5% NO/He for 10 min followed by He flow (orange) for 10 min at 200 °C; and variations in the intensities of peaks attributed to surface nitrite species and the as-detected concentrations of N_2O and CO_2 (products) during the reactions.

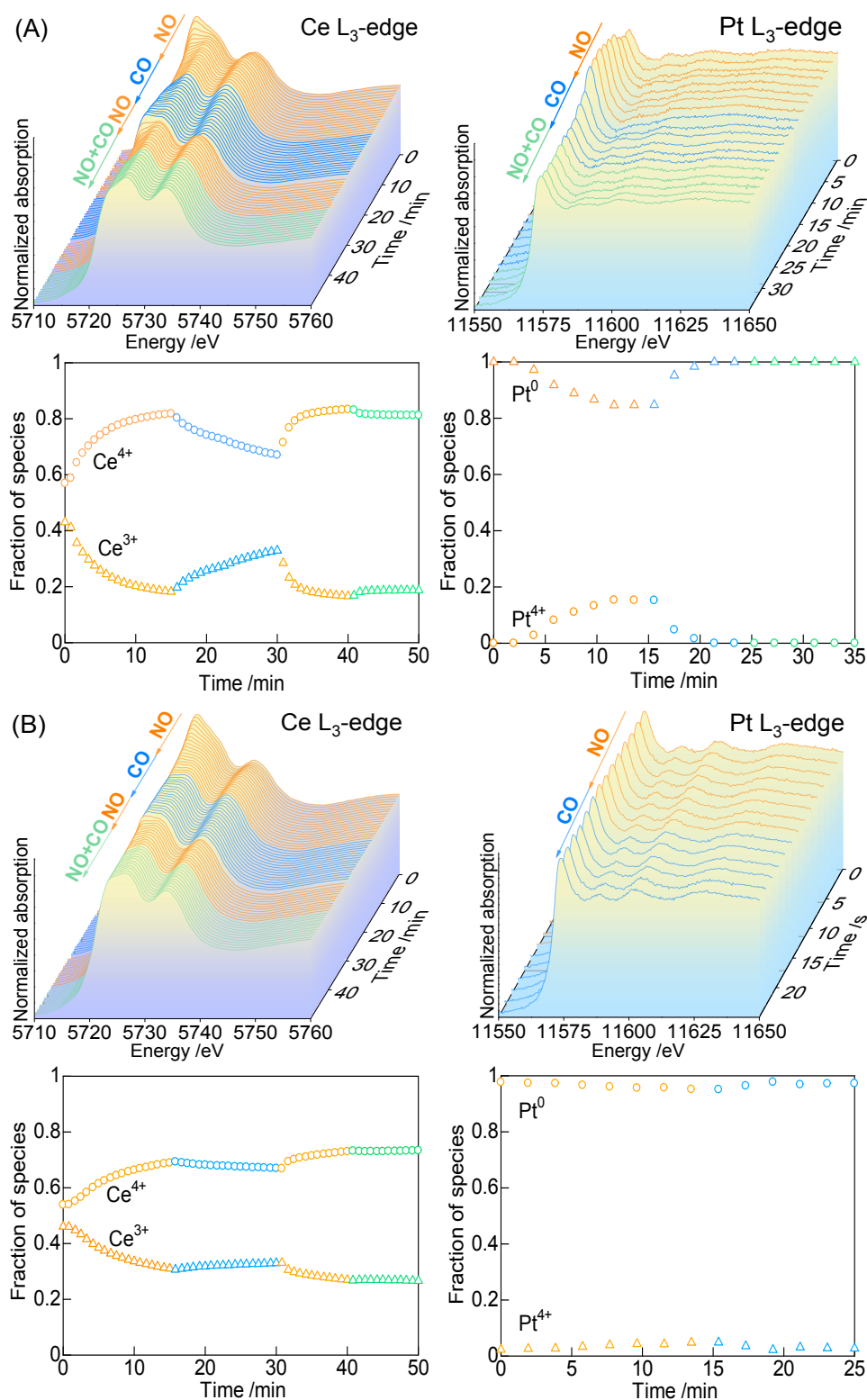


Figure 8. *In situ* Ce and Pt L₃-edge XAS measurements during NO–CO reactions on (A) fresh and (B) aged Pt/OSM(66%CeO₂) (Sample amount = 2.0 mg with 20.4 mg of BN for Ce L₃-edge and 21.8 mg with 12.8 mg of BN for Pt L₃-edge measurements) in a switched flow of 0.5% NO/He, 0.5% CO/He or 0.5%NO+0.5%CO/He (1000 mL/min) at 200 °C following reduction using H₂ at 400 °C, using CeO₂ and Ce(NO₃)₃, and Pt foil and PtO₂ as references for linear combination fitting analysis.

3.3 Catalytic evaluation of monolithic honeycomb catalysts under TWC conditions

The effect of OSMs on TWC light-off performance over monolithic honeycombs of fresh and aged Pt/OSMs was investigated in the light-off mode in a switched gas flow with a lambda perturbation of 1 Hz between 0.95 (rich) and 1.05 (lean) at SV = 100,000 h⁻¹, as shown in **Figure 9**. The honeycomb catalyst was pretreated in a flow of gas having an identical composition to that used in the evaluation at 400 °C for 30 min prior to each test. The continuously monitored performance of the fresh Pt/OSMs in the removal of NO, CO, and C₃H₆ increased with the increase in the ceria content in the OSM support, attributing to the promotion of ceria in the formation of nitrite species and their reactivity toward CO and C₃H₆. However, the conversion of NO, CO, and C₃H₆ on aged Pt/OSMs followed the order Pt/OSM(66%CeO₂) > Pt/OSM(45%CeO₂) > Pt/OSM(20%CeO₂) > Pt/OSM(100%CeO₂) considering the promoting effect of ceria, the decreased redox abilities of Pt and Ce species, and the sintering of the OSM supports during the ageing treatment ensured by *in situ / operando* XAS and IR as well as N₂ adsorption and XRD characterizations. Although the three-way catalysis activity of Pt/OSMs decreased dramatically following the ageing treatment, it is a vital investigation for practical applications, as catalysts are exposed to extremely harsh conditions that they must withstand for extended periods^{97,98}. In addition, we correlated the ceria content with the T₂₀ behavior, which was defined as the temperature at which the conversion was 20%, to further demonstrate the effect of OSMs on three-way catalysis performance, as presented in **Figure S11**. In fresh catalysts, T₂₀ decreases with increasing ceria content, indicating that the ceria in OSM facilitates the conversion of NO, CO, and C₃H₆ on supported Pt TWCs at lower temperatures. In contrast, Pt/OSM(66%CeO₂) exhibited the lowest T₂₀ among the aged catalysts, because of its good thermal stability improved by the introduction of zirconia and relatively high catalytic activity promoted by the ceria.

Figure 10 shows the effect of OSMs on the lambda-sweep performance over monolithic honeycomb Pt/OSM catalysts in the range of 0.95 (rich) to 1.05 (lean) at increments of 0.01 at 300 °C, during which the conversions of NO, CO and C₃H₆ were recorded after maintaining each lambda step for 60 s to examine the steady-state activity. The conversion of NO occurs efficiently in the rich region (0.95 ≤ λ < 1), wherein excess reducing gas components are present. The NO removal efficiency increased with the increase in the ceria content for fresh Pt/OSMs; however, Pt/OSM(66%CeO₂)

exhibited the highest efficiency among the aged catalysts, which is in agreement with the results of the light-off performance test. The conversion of CO and C₃H₆ is sufficient in the lean region ($1 < \lambda \leq 1.05$), where oxidation processes are preferred in the presence of abundant O₂. All of the fresh Pt/OSMs exhibited identical maximum removal efficiencies for CO and C₃H₆; however, only Pt/OSM(66%CeO₂) retained high activity among the aged catalysts. The removal efficiencies of CO and C₃H₆ on fresh Pt/OSMs also increased with increasing ceria content in the rich region. These results are in agreement with the aforementioned investigations and demonstrate that the high ceria content together with the excellent redox properties of Pt and Ce species, which are suppressed following the ageing treatment of Pt/OSM catalysts, promote three-way catalysis. In addition, interesting behaviors are exhibited by the aged catalysts: the NO conversion is lower under rich conditions compared to that under lean conditions, particularly for aged Pt/OSM(20%CeO₂). This is directly opposite to the normal reactivity of NO, as it is an oxidant that reacts with a reductant under reducing conditions. This can be explained by the poisoning effect of CO. Under rich conditions, CO poisoning drastically reduces the NO conversion, while under lean conditions, the CO poisoning is weaker, and consequently the activity is higher. This is also consistent with the fact that the aged Pt/OSM(20%CeO₂) catalyst exhibited the lowest apparent reaction order with respect to CO in the NO–CO reaction. This phenomenon originating from strong CO poisoning is peculiar to Pt and is not seen in Rh and Pd, and it is essential to account for it during the development of Pt-based TWCs. When the reaction temperature was increased to 400 °C (**Figure S12**) and thereafter to 500 °C (**Figure S13**), the conversion of NO, CO, and C₃H₆ on fresh and aged Pt/OSMs was remarkably enhanced, and the differences between the catalytic performances of these catalysts decreased gradually.

The lambda value significantly fluctuates from low (rich) to high (lean) during the modern practical TWC process due to an engine fuel-cut operation which was introduced relatively recently to improve fuel efficiency^{99,100}, so it is important that the TWC catalysts possess a broad working window and efficiently remove exhaust gases under such turbulent conditions^{83,101}. Therefore, the effect of OSMS on TWC lambda-switching performance over Pt/OSM-coated honeycomb catalysts was investigated, and the continuously recorded conversions of NO, CO, and C₃H₆ are shown in **Figure 11**. The catalyst

was pretreated under lean conditions ($\lambda = 1.05$) at 300 °C for 5 min prior to the commencement of the test under rich conditions ($\lambda = 0.95$), followed by switching to lean conditions and then to rich conditions again. There are detection delays for NO and CO relative to C_3H_6 due to the experimental setup (1.0 s for NO and 3.2 s for CO relative to C_3H_6). For the fresh Pt/OSMs, a high NO conversion was retained for the longest duration over Pt/OSM(100%CeO₂), whereas the NO conversion declined faster than for the other catalysts that had lower ceria contents. The NO conversion occurred nearly identically over the catalysts studied for the subsequent change from lean to rich, followed by a gradual decrease in the conversion for Pt/OSM(20%CeO₂) and Pt/OSM(45%CeO₂). A similar gradual decrease in the conversions under rich conditions was also observed for CO and C_3H_6 . This was probably caused by CO, which acts as a poison for Pt, as observed during the NO–CO reactions. The reactivities of the aged Pt/OSMs were much lower for all the reactants than that of the fresh Pt/OSMs. The increase in the conversion of NO under lean conditions was also observed here, particularly for aged Pt/OSM(20%CeO₂). This phenomenon can also be explained by the strong poisoning effect of CO under rich conditions, causing the extremely low NO conversion.

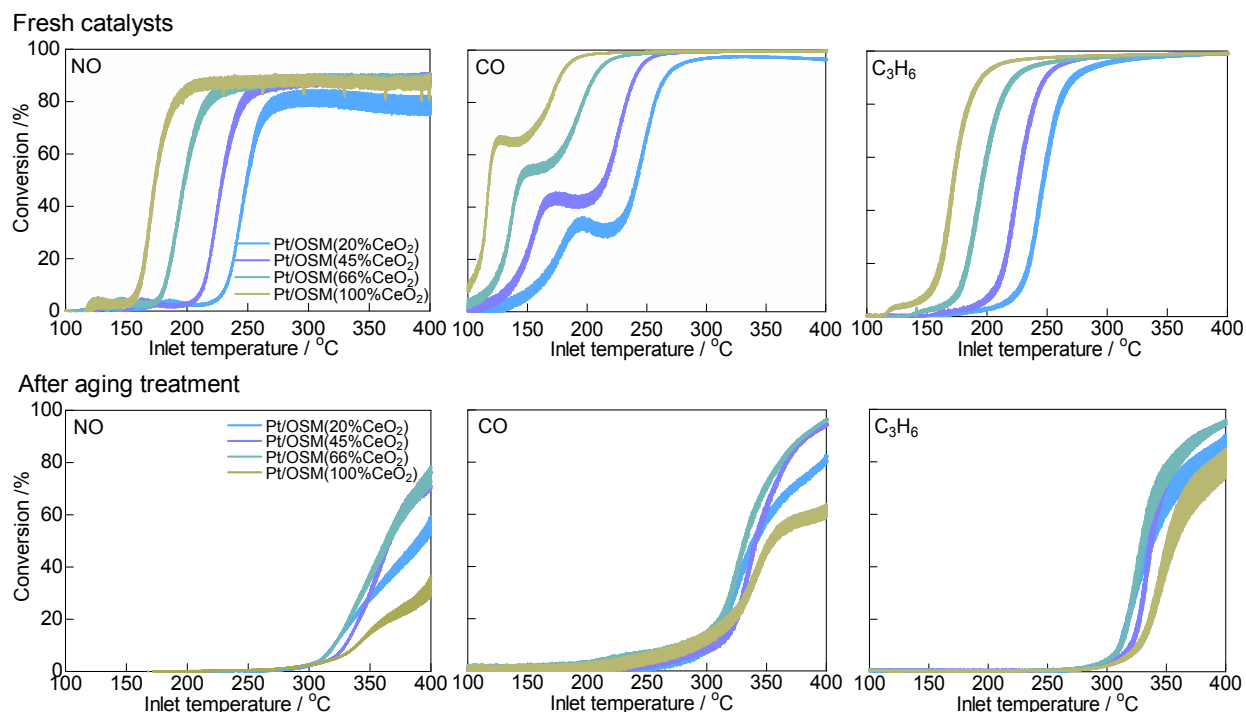


Figure 9. Effect of OSMs on TWC light-off performance over fresh and aged Pt/OSM-coated honeycomb catalysts under a switched flow of CO (2.4-0.6%), C_3H_6 (420 ppm), H_2 (0.8-0.2%), NO (1000 ppm), O_2 (0.6-1.65%), CO_2 (15%) and H_2O (10%) (with the balance being composed of N_2) with lambda perturbation of 1 Hz between 0.95 (rich) and 1.05 (lean) at a heating rate of 25 °C/min and $SV = 100,000\ h^{-1}$.

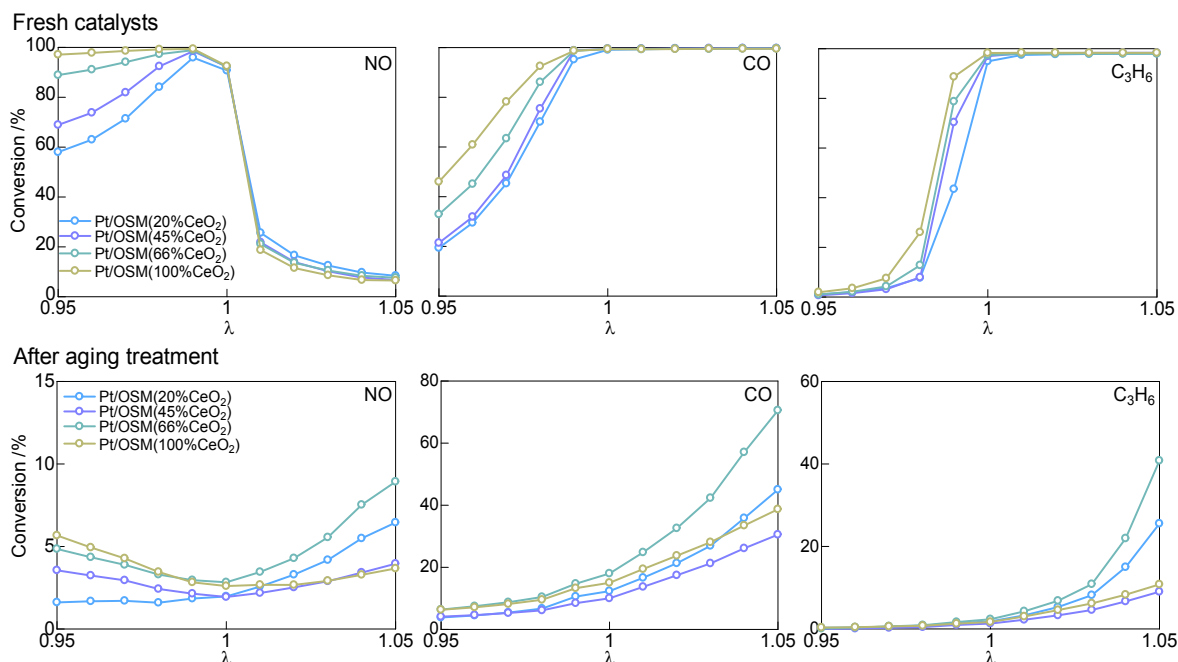


Figure 10. Effect of OSMs on TWC lambda-sweep performance over fresh and aged Pt/OSM-coated honeycomb catalysts under a switched flow of CO (2.4-0.6%), C₃H₆ (420 ppm), H₂ (0.8-0.2%), NO (1000 ppm), O₂ (0.6-1.65%), CO₂ (15%), and H₂O (10%) (with the balance being composed of N₂) with the lambda perturbation interval set at 60 s and changing from 0.95 (rich) to 1.05 (lean) through steps of 0.01 at 300 °C and SV = 100,000 h⁻¹.

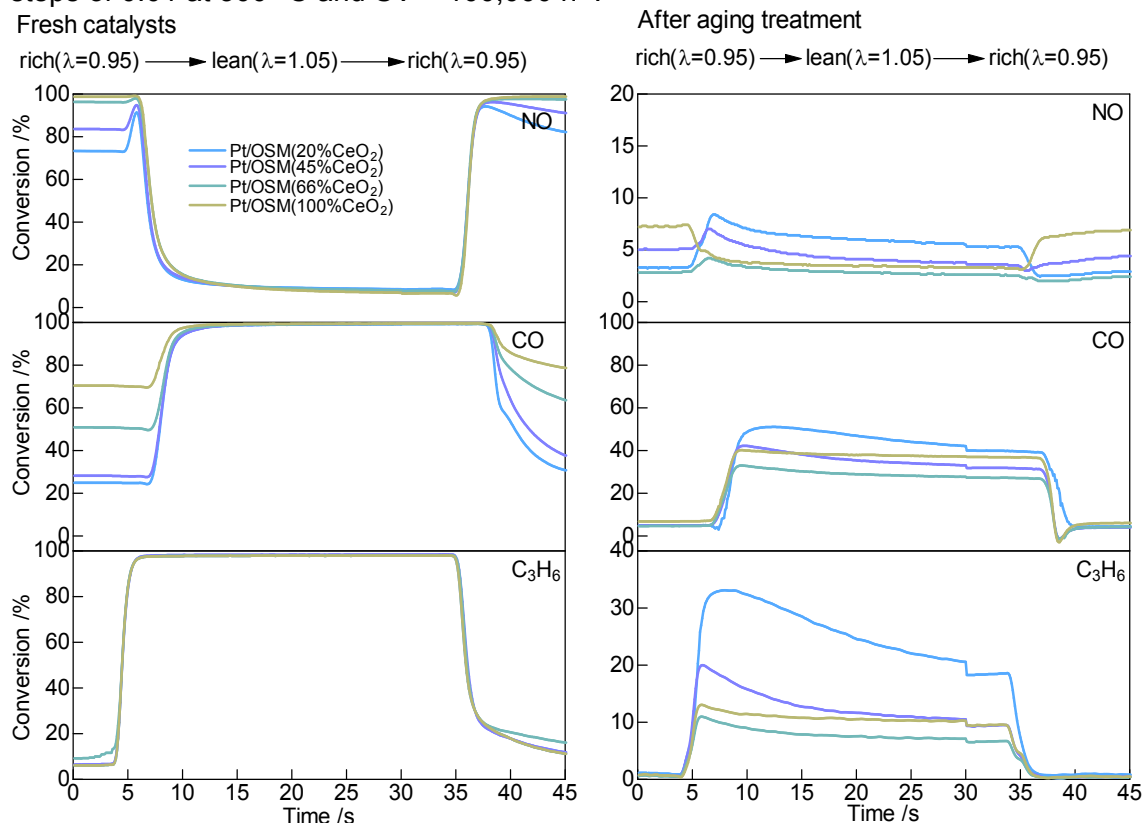


Figure 11. Effect of OSMs on TWC lambda-switching performance over fresh and aged Pt/OSMs-coated honeycomb catalysts under a switched flow of CO (2.4-0.6%), C₃H₆ (420 ppm), H₂ (0.8-0.2%), NO (1000 ppm), O₂ (0.6-1.65%), CO₂ (15%), and H₂O (10%) (with the balance being composed of N₂) with the lambda perturbation interval set at 30 s and changing between 0.95 (rich) and 1.05 (lean) at 300 °C and SV = 100,000 h⁻¹. Note that there are detection delays due to the experimental setup (1.0 s for NO and 3.2 s for CO relative to C₃H₆).

Conclusions

In this study, we investigated the effect of OSMs on the performance of Pt-based TWCs using a combination of spectroscopic and kinetic measurements. The catalytic evaluations of powdered as well as monolithic honeycomb catalysts showed that Pt/OSM(100%CeO₂) and Pt/OSM(66%CeO₂) exhibited the highest NO conversion among their corresponding fresh and aged sample series. *Operando* and *in situ* CO adsorption IR spectroscopic experiments as well as XPS characterizations revealed that increasing the ceria content of the OSM support promoted not only the production of nitrite species and their reactivity toward CO reactant but also the formation of more electron-deficient Pt⁰ species, which results in high performance in the three-way catalysis process and effective resistance to CO poisoning over fresh Pt/OSM catalysts. *In situ* XAS measurements confirmed that both Pt and Ce species in the Pt/OSM catalyst were involved in the TWC reactions through their redox cycles. However, the hydrothermal ageing treatment caused the sintering of the Pt particles and the lattice contraction of CeO₂ in Pt/OSMs. This severely retarded the redox behavior of Pt and Ce species and reduced the promoting effect of ceria, thereby reducing the catalytic activity of the aged catalysts at relatively low temperatures compared to their fresh counterparts. In addition, the strong poisoning of the Pt catalysts, particularly after hydrothermal ageing during the rich operation, which was more significant than that for Rh and Pd catalysts, should be considered when developing Pt-based TWCs.

ACKNOWLEDGEMENTS

This study was financially supported by KAKENHI (Grant No. 20H02518, 20H02775, 20KK0111, 20F20345, and 21K18185) from the Japan Society for the Promotion of Science (JSPS) and by the Japanese Ministry of Education, Culture, Sports, Science, and Technology (MEXT) within the projects “Integrated Research Consortium on Chemical Sciences (IRCCS)” and “Elements Strategy Initiative to Form Core Research Center” (JPMXP0112101003). This study was also supported by the JST-CREST project JPMJCR17J3. G.W. acknowledges a JSPS postdoctoral fellowship (No. P20345). The authors thank the technical division of the Institute for Catalysis (Hokkaido University) for manufacturing experimental equipment as well as the technical staff at the Open Facility of Hokkaido

University for their assistance with STEM observations. XAS measurements were conducted at the BL-14B2 beamline of SPring-8 at JASRI (proposal number 2019B1686 and 2020A1695).

REFERENCES

- 1 X. Zhu, K. Li, L. Neal and F. Li, *ACS Catal.*, 2018, **8**, 8213–8236.
- 2 C. Huang, W. Shan, Z. Lian, Y. Zhang and H. He, *Catal. Sci. Technol.*, 2020, **10**, 6407–6419.
- 3 J. Lee, J. R. Theis and E. A. Kyriakidou, *Appl. Catal. B Environ.*, 2019, **243**, 397–414.
- 4 J. Wang, H. Chen, Z. Hu, M. Yao and Y. Li, *Catal. Rev.*, 2015, **57**, 79–144.
- 5 H. Jeong, O. Kwon, B. S. Kim, J. Bae, S. Shin, H. E. Kim, J. Kim and H. Lee, *Nat. Catal.*, 2020, **3**, 368–375.
- 6 A. K. Datye and M. Votsmeier, *Nat. Mater.*, DOI:10.1038/s41563-020-00805-3.
- 7 M. Machida, Y. Uchida, S. Iwashita, H. Yoshida, M. Tsushida, J. Ohyama, Y. Nagao, Y. Endo and T. Wakabayashi, *ACS Catal.*, 2021, **11**, 9462–9470.
- 8 K. Ueda, J. Ohyama and A. Satsuma, *ACS Omega*, 2017, **2**, 3135–3143.
- 9 M. Machida, Y. Uchida, S. Iwashita, H. Yoshida, M. Tsushida, J. Ohyama, Y. Nagao, Y. Endo and T. Wakabayashi, *ACS Catal.*, 2021, 9462–9470.
- 10 H. Asakura, M. Kirihara, K. Fujita, S. Hosokawa, S. Kikkawa, K. Teramura and T. Tanaka, *Ind. Eng. Chem. Res.*, 2020, **59**, 19907–19917.
- 11 L. Savereide, A. Gosavi, K. E. Hicks and J. M. Notestein, *J. Catal.*, 2020, **381**, 355–362.
- 12 Y. Renème, F. Dhainaut, M. Trentesaux, B. Ravanbakhsh, P. Granger, C. Dujardin, L. Gengembre and P. L. De Cola, *Surf. Interface Anal.*, 2010, **42**, 530–535.
- 13 Y. Renème, F. Dhainaut and P. Granger, *Appl. Catal. B Environ.*, 2012, **111–112**, 424–432.
- 14 Y. Renème, F. Dhainaut, Y. Schuurman, C. Mirodatos and P. Granger, *Appl. Catal. B Environ.*, 2014, **160–161**, 390–399.

- 15 M. Machida, A. Fujiwara, H. Yoshida, J. Ohyama, H. Asakura, S. Hosokawa, T. Tanaka, M. Haneda, A. Tomita, T. Miki, K. Iwashina, Y. Endo, Y. Nakahara, S. Minami, N. Kato, Y. Hayashi, H. Goto, M. Hori, T. Tsuda, K. Miura, F. Kimata and K. Iwachido, *ACS Catal.*, 2019, **9**, 6415–6424.
- 16 L. Li, N. Zhang, X. Huang, Y. Liu, Y. Li, G. Zhang, L. Song and H. He, *ACS Catal.*, 2018, **8**, 3222–3231.
- 17 J. Gong, D. Wang, J. Li, N. Currier and A. Yezerets, *Appl. Catal. B Environ.*, 2017, **203**, 936–945.
- 18 M. A. Salaev, A. A. Salaeva, T. S. Kharlamova and G. V. Mamontov, *Appl. Catal. B Environ.*, 2021, **295**, 120286.
- 19 H. Asakura, S. Hosokawa, K. Beppu, K. Tamai, J. Ohyama, T. Shishido, K. Kato, K. Teramura and T. Tanaka, *Catal. Sci. Technol.*, 2021, **11**, 6182-6190.
- 20 L. Zhang, I. A. W. Filot, Y. Q. Su, J. X. Liu and E. J. M. Hensen, *J. Catal.*, 2018, **363**, 154–163.
- 21 M. Grünbacher, A. Tarjomannejad, P. D. K. Nezhad, C. Praty, K. Ploner, A. Mohammadi, A. Niaei, B. Klötzer, S. Schwarz, J. Bernardi, A. Farzi, M. J. I. Gómez, V. T. Rivero and S. Penner, *J. Catal.*, 2019, **379**, 18–32.
- 22 M. Salaün, A. Kouakou, S. Da Costa and P. Da Costa, *Appl. Catal. B Environ.*, 2009, **88**, 386–397.
- 23 S. B. Kang, I. S. Nam, B. K. Cho, C. H. Kim and S. H. Oh, *Chem. Eng. J.*, 2015, **278**, 328–338.
- 24 H. S. Gandhi, G. W. Graham and R. W. McCabe, *J. Catal.*, 2003, **216**, 433–442.
- 25 C. Coney, C. Hardacre, K. Morgan, N. Artioli, A. P. E. York, P. Millington, A. Kolpin and A.

- Goguet, *Appl. Catal. B Environ.*, 2019, **258**, 117918.
- 26 V. Meeyoo, D. L. Trimm and N. W. Cant, *Appl. Catal. B Environ.*, 1998, **16**, L101–L104.
- 27 M. Hatanaka, N. Takahashi, T. Tanabe, Y. Nagai, K. Dohmae, Y. Aoki, T. Yoshida and H. Shinjoh, *Appl. Catal. B Environ.*, 2010, **99**, 336–342.
- 28 S. Andonova, Z. Aybegüm Ok, N. Drenchev, E. Ozensoy and K. Hadjiivanov, *J. Phys. Chem. C*, 2018, **122**, 12850–12863.
- 29 D. Ausgabe, M. Hirose, N. Ishiguro, K. Shimomura, N. Burdet, H. Matsui, M. Tada and Y. Takahashi, *Angew. Chem. Int. Ed.*, 2018, **130**, 1490–1495.
- 30 M. Ozawa, M. Misaki, M. Iwakawa, M. Hattori, K. Kobayashi, K. Higuchi and S. Arai, *Catal. Today*, 2019, **332**, 251–258.
- 31 K. I. Muto, N. Katada and M. Niwa, *Appl. Catal. A Gen.*, 1996, **134**, 203–215.
- 32 T. Toyao, Y. Jing, K. Kon, T. Hayama, S. Nagaoka and K. Shimizu, *Chem. Lett.*, 2018, **47**, 1036–1039.
- 33 A. A. Vedyagin, R. M. Kenzhin, Mikhail, Y. Tashlanov, E. A. Alikin, V. O. Stoyanovskii, P. E. Plyusnin, Y. V Shubin, I. V Mishakov, M. Y. Smirnov, Alexander, V. Kalinkin, Valerii and I. Bukhtiyarov, *Top. Catal.*, 1234, **63**, 152–165.
- 34 H. Asakura, S. Hosokawa, T. Ina, K. Kato, K. Nitta, K. Uera, T. Uruga, H. Miura, T. Shishido, J. Ohyama, A. Satsuma, K. Sato, A. Yamamoto, S. Hinokuma, H. Yoshida, M. Machida, S. Yamazoe, T. Tsukuda, K. Teramura and T. Tanaka, *J. Am. Chem. Soc.*, 2017, **140**, 176–184.
- 35 M. Wang, P. Dimopoulos Eggenschwiler, T. Franken, D. Ferri and O. Kröcher, *Chem. Eng. J.*, 2021, **422**, 129932.

- 36 S. Keav, S. Matam, D. Ferri and A. Weidenkaff, *Catalysts*, 2014, **4**, 226–255.
- 37 G. C. M. Rodríguez, K. Kelm, S. Heikens, W. Grünert and B. Saruhan, *Catal. Today*, 2012, **184**, 184–191.
- 38 M. Alifanti, B. Baps, N. Blangenois, J. Naud, P. Grange and B. Delmon, *Chem. Mater.*, 2002, **15**, 395–403.
- 39 L. F. Liotta, A. Macaluso, A. Longo, G. Pantaleo, A. Martorana and G. Deganello, *Appl. Catal. A Gen.*, 2003, **240**, 295–307.
- 40 A. I. Kozlov, H. K. Do, A. Yezerets, P. Andersen, H. H. Kung and M. C. Kung, *J. Catal.*, 2002, **209**, 417–426.
- 41 H. He, H. X. Dai, L. H. Ng, K. W. Wong and C. T. Au, *J. Catal.*, 2002, **206**, 1–13.
- 42 P. Li, X. Chen, Y. Li and J. W. Schwank, *Catal. Today*, 2019, **327**, 90–115.
- 43 F. Dong, T. Tanabe, N. Takahashi and H. Shinjoh, *Catal. Today*, 2019, **332**, 259–266.
- 44 J. Wu, A. E. O'Neill, C. H. Li, J. R. Jinschek and G. Cavataio, *Appl. Catal. B Environ.*, 2021, **280**, 119450.
- 45 R. Kopelent, A. Tereshchenko, A. Guda, G. Smolentsev, L. Artiglia, V. L. Sushkevich, A. Bugaev, I. I. Sadykov, T. Baidya, M. Bodnarchuk, J. Anton van Bokhoven, M. Nachtgeal and O. V. Safonova, *ACS Catal.*, 2021, **11**, 9435–9449.
- 46 T. Yamamoto, A. Suzuki, Y. Nagai, T. Tanabe, F. Dong, Y. Inada, M. Nomura, M. Tada, Y. Iwasawa, *Angew. Chem. Int. Ed.*, 2007, **119**, 9413–9416.
- 47 E. V. Kondratenko, Y. Sakamoto, K. Okumura and H. Shinjoh, *Appl. Catal. B Environ.*, 2009, **89**, 476–483.

- 48 H. Shang, Y. Wang, Y. Cui, R. Fang, W. Hu, M. Gong and Y. Chen, *Chinese J. Catal.*, 2015, **36**, 290–298.
- 49 R. Schmitt, A. Nanning, O. Kraynis, R. Korobko, A. I. Frenkel, I. Lubomirsky, S. M. Haile and J. L. M. Rupp, *Chem. Soc. Rev.*, 2020, **49**, 554.
- 50 A. Kubacka, A. Iglesias-Juez, M. Di Michiel, M. A. Newton and M. Fernández-García, *Phys. Chem. Chem. Phys.*, 2013, **15**, 8640.
- 51 J. Rink, N. Meister, F. Herbst and M. Votsmeier, *Appl. Catal. B Environ.*, 2017, **206**, 104–114.
- 52 F. Dong, A. Suda, T. Tanabe, Y. Nagai, H. Sobukawa, H. Shinjoh, M. Sugiura, C. Descorme and D. Duprez, *Catal. Today*, 2004, **93–95**, 827–832.
- 53 A. Laachir, V. Perrichon, S. Bernal, J. J. Calvino and G. A. Cifredo, *J. Mol. Catal.*, 1994, **89**, 391–396.
- 54 G. R. Rao, J. Kagpar, S. Meriani, R. Di Monte and M. Graziani, *Catal. Lett.*, 1994, **24**, 107–112.
- 55 C. Li, Q. Xin, X. Gao and T. Onishi, *Stud. Surf. Sci. Catal.*, 1993, **75**, 1955–1958.
- 56 L. Kqpihski, M. Wdycz and J. Okal, *J. Chem. Soc., Faraday Trans.*, 1995, **91**, 507–515.
- 57 T. W. van Deelen, C. Hernández Mejía and K. P. de Jong, *Nat. Catal.*, 2019, **2**, 955–970.
- 58 T. Wakita and M. Yashima, *Appl. Phys. Lett.*, 2008, **92**, 101921.
- 59 J. Fan, X. Wu, R. Ran and D. Weng, *Appl. Surf. Sci.*, 2005, **245**, 162–171.
- 60 Y. Nagai, T. Hirabayashi, K. Dohmae, N. Takagi, T. Minami, H. Shinjoh and S. Matsumoto, *J. Catal.*, 2006, **242**, 103–109.
- 61 J. G. Nunan, H. J. Robota, M. J. Cohn and S. A. Bradley, *J. Catal.*, 1992, **133**, 309–324.
- 62 S. T. Oyama, X. Zhang, J. Lu, Y. Gu and T. Fujitani, *J. Catal.*, 2008, **257**, 1–4.

- 63 M. Rothensteiner, A. Bonk, U. F. Vogt, H. Emerich and J. A. Van Bokhoven, *J. Phys. Chem. C*, 2016, **120**, 13931–13941.
- 64 N. Izu, H. Kishimoto, T. Omata, K. Ono and S. Otsuka-Yao-Matsuo, *Sci. Technol. Adv. Mater.*, 2001, **2**, 397–404.
- 65 F. Zhang, C. H. Chen, J. C. Hanson, R. D. Robinson, I. P. Herman and S. W. Chan, *J. Am. Ceram. Soc.*, 2006, **89**, 1028–1036.
- 66 M. Pijolat, M. Prin, M. Soustelle, O. Touret and P. Nortier, *J. Chem. Soc., Faraday Trans.*, 1995, **91**, 3941–3948.
- 67 P. Nachimuthu, W. C. Shih, R. S. Liu, L. Y. Jang and J. M. Chen, *J. Solid State Chem.*, 2000, **149**, 408–413.
- 68 C. Paun, O. V. Safonova, J. Szlachetko, P. M. Abdala, M. Nachtegaal, J. Sa, E. Kleymentov, A. Cervellino, F. Krumeich and J. A. van Bokhoven, *J. Phys. Chem. C*, 2012, **116**, 7312–7317.
- 69 L. M. Toscani, A. F. Craievich, M. C. A. Fantini, D. G. Lamas and S. A. Larrondo, *J. Phys. Chem. C*, 2016, **120**, 24165–24175.
- 70 H. C. Yao and Y. F. Y. Yao, *J. Catal.*, 1984, **86**, 254–265.
- 71 M. F. L. Johnson and J. Mooi, *J. Catal.*, 1987, **103**, 502–505.
- 72 Y. Madier, C. Descorme, A. M. Le Govic and D. Duprez, *J. Phys. Chem. B*, 1999, **103**, 10999–11006.
- 73 G. Balducci, J. Kašpar, P. Fornasiero, M. Graziani, M. S. Islam and J. D. Gale, *J. Phys. Chem. B*, 1997, **101**, 1750–1753.
- 74 J. Kašpar, P. Fornasiero and M. Graziani, *Catal. Today*, 1999, **50**, 285–298.

- 75 X. Wu, J. Fan, R. Ran and D. Weng, *Chem. Eng. J.*, 2005, **109**, 133–139.
- 76 W. Karim, C. Spreafico, A. Kleibert, J. Gobrecht, J. VandeVondele, Y. Ekinici and J. A. van Bokhoven, *Nature*, 2017, **541**, 68–71.
- 77 M. F. Luo and X. M. Zheng, *Appl. Catal. A Gen.*, 1999, **189**, 15–21.
- 78 P. Fornasiero, R. Di Monte, G. R. Rao, J. Kaspar, S. Meriani, A. Trovarelli and M. Graziani, *J. Catal.*, 1995, **151**, 168–177.
- 79 P. Bazin, O. Saur, J. C. Lavalley, M. Daturi and G. Blanchard, *Phy. Chem. Chem. Phy.* 2005, **7**, 187–194.
- 80 M. Gajdo, A. Eichler and J. Hafner, *J. Phys. Condens. Matter*, 2004, **16**, 1141–1164.
- 81 C. D. Zeinalipour-Yazdi, A. L. Cooksy and A. M. Efstathiou, *Surf. Sci.*, 2008, **602**, 1858–1862.
- 82 I. Z. Koleva, H. A. Aleksandrov and G. N. Vayssilov, *Catal. Today*, 2020, **357**, 442–452.
- 83 Y. Jing, Z. Cai, C. Liu, T. Toyao, Z. Maeno, H. Asakura, S. Hiwasa, S. Nagaoka, H. Kondoh and K. I. Shimizu, *ACS Catal.*, 2020, **10**, 1010–1023.
- 84 Y. Jing, G. Wang, K. Wei Ting, Z. Maeno, K. Oshima, S. Satokawa, S. Nagaoka, K. Shimizu and T. Toyao, *J. Catal.*, 2021, **400**, 387–396.
- 85 I. V. Yentekakis, P. Vernoux, G. Goula and A. Caravaca, *Catalysts*, 2019, **9**, 1–72.
- 86 A. Gremminger, J. Pihl, M. Casapu, J. D. Grunwaldt, T. J. Toops and O. Deutschmann, *Appl. Catal. B Environ.*, 2020, **265**, 118571.
- 87 P. T. Fanson, M. R. Horton, W. N. Delgass and J. Lauterbach, *Appl. Catal. B Environ.*, 2003, **46**, 393–413.
- 88 W. A. Brown and D. A. King, *J. Phys. Chem. B*, 2000, **104**, 2578–2595.

- 89 C. Sedlmair, K. Seshan, A. Jentys and J. A. Lercher, *J. Catal.*, 2003, **214**, 308–316.
- 90 I. Nova, L. Castoldi, L. Lietti, E. Tronconi, P. Forzatti, F. Prinetto and G. Ghiotti, *J. Catal.*, 2004, **222**, 377–388.
- 91 T. W. van Deelen, C. H. Mejía and K. P. de Jong, *Nat. Catal.*, 2019, **2**, 955–970.
- 92 L. Lietti, M. Daturi, V. Blasin-Aubø, G. Ghiotti, F. Prinetto and P. Forzatti, *ChemCatChem*, 2012, **4**, 55–58.
- 93 V. R. Choudhary, K. R. Srinivasan and A. P. Singh, *Zeolites*, 1990, **10**, 16–20.
- 94 A. Trovarelli, *Catal. Rev. Sci. Eng.*, 1996, **38**, 439–520.
- 95 Y. Nagai, K. Dohmae, Y. Ikeda, N. Takagi, T. Tanabe, N. Hara, G. Guilera, S. Pascarelli, M. A. Newton, O. Kuno, H. Jiang, H. Shinjoh and S. Matsumoto, *Angew. Chem. Int. Ed.* 2008, **47**, 9303–9306.
- 96 A. M. Gänzler, M. Casapu, F. Maurer, H. Störmer, D. Gerthsen, G. Ferré, P. Vernoux, B. Bornmann, R. Frahm, V. Murzin, M. Nachtegaal, M. Votsmeier and J. D. Grunwaldt, *ACS Catal.*, 2018, **8**, 4800–4811.
- 97 M. Haneda, Y. Nakamura, T. Yamada, S. Minami, N. Kato, K. Iwashina, Y. Endo, Y. Nakahara and K. Iwachido, *Catal. Sci. Technol.*, 2021, **11**, 912–922.
- 98 A. Fujiwara, Y. Tsurunari, H. Yoshida, J. Ohyama, T. Yamada, M. Haneda, T. Miki and M. Machida, *ACS Omega*, 2020, **5**, 28897–28906.
- 99 M. Machida, M. Ueno, T. Omura, S. Kurusu, S. Hinokuma, T. Nanba, O. Shinozaki and H. Furutani, *Ind. Eng. Chem. Res.*, 2017, **56**, 3184–3193.
- 100 M. Choi, J. Song, E. Lee, S. Ma, S. Lee, J. Seo, S. Yoo and J. Lee, *SAE Tech. Pap.*, 2019, **1**,

1292.

- 101 M. Machida, M. Ueno, T. Omura, S. Kurusu, S. Hinokuma, T. Nanba, O. Shinozaki and H. Furutani, *Ind. Eng. Chem. Res.* 2017, **56**, 3184–3193.